Dynamic Modular Modeling of Smart Loads Associated With Electric Springs and Control

Tianbo Yang, *Student Member, IEEE*, Tao Liu, *Member, IEEE*, Jie Chen, *Student Member, IEEE*, Shuo Yan, *Member, IEEE*, and S.Y. Ron Hui, *Fellow, IEEE*

***Abstract*—Smart loads associated with electric springs (ES) have been used for fast demand-side management for smart grid. While simplified dynamic ES models have been used for power system simulation, these models do not include the dynamics of the power electronic circuits and control of the ES. This paper presents a dynamic and modular ES model that can incorporate the controller design and the dynamics of the power electronic circuits. Based on experimental measurements, the order of this dynamic model has been reduced so that the model suits both circuit and system simulations. The model is demonstrated with the radial-chordal decomposition controller for both voltage and frequency regulation. The modular approach allows the circuit and controller of the ES model and the load module to be combined in the *d–q* frame. Experimental results based on single and multiple smart loads setup are provided to verify the results obtained from the model simulation. Then, the ES model is incorporated into power system simulations including an IEEE 13 node power system and a three-phase balanced microgrid system.**

***Index Terms*—Electric spring, microgrids, parameter estimation, radial-chordal decomposition (RCD), smart loads.**

I. Introduction

INCREASING use of renewable energy such as solar and wind power has posed new technical challenges in maintaining balance between power supply and demand. In order to reduce power imbalance, technologies, such as energy storage [1], [2], advanced control strategy [3], and scheduling delay-tolerant power demand tasks through directly load control or indirectly pricing influence [4], [5], have been broadly discussed.

Recently, electric spring (ES) has been proposed as a fast demand response technology to tame the disturbance arising from high penetration of renewable energy into ac power grids [6], [7]. The original ES (ES-1) was demonstrated to mitigate mains voltage fluctuation caused by intermittent renewable energy using reactive power compensation. By controlling the output voltage of the ES, the voltage of a noncritical load in series with the ES is adjusted. In such a way, the ES and the noncritical load form a smart load that can interact with the grid by providing reactive power compensation directly through the ES and active power compensation indirectly through the modulation of the noncritical load power. The ability of ES was later enhanced in the second version (ES-2) with both direct active and reactive power compensation functions. In [8], the capacitors in dc-link of ES-1 are replaced by batteries to form the ES-2. The use of batteries provides the ES with the ability of both releasing and absorbing active power, so that power exchange in four-quadrants through the ES becomes possible. Yan *et al*. [9] further broaden the operation area of ES with back-to-back topology. In [10] and [11], different ES control strategies for voltage compensation with active/reactive power are reported. The shunt type of ES with battery management is discussed in [12], while [13] demonstrates the use of ES as an active power filter against harmonic distortion. Three-phase ES has been developed for reducing power imbalance in addition to voltage and frequency regulation [14]. Furthermore, a distributed control strategy for a group of smart loads embedded with ES is discussed in [15].

As the main use of ES is to stabilize the power grid against disturbance caused by the injection of intermittent renewable power, it is necessary to develop ES model that is suitable for power system simulation study. The first contribution to the dynamic modeling of ES is reported in [16]. Based on the first version of ES, it represents the ES as a controllable voltage source with the current vector perpendicular to the output voltage vector. Its advantage lies in the model simplicity without the details of the power electronics. Hence, the dynamic nature of the smart loads embedded with ES is largely ignored.

With recent advancements in both ES topologies and control, there is a need for more versatile model that can cope with the dynamics of the ES circuit and its controller design and different types of loads associated with the ES. This paper presents a new dynamic modular model of the smart load associated with an ES and its controller. A theoretical analysis and model parameter estimation method are included to formulate the dynamic model. There are three modules in the proposed model, namely the inner model, the outer controller, and the load model. The full structure of the proposed model is shown in Fig. 1, where $V_{\rm g}$, $V_{\rm g}^*$, ${\varphi_{\rm sl}}^*$, $V_{\rm es}$, $V_{\rm es}^*$, $I_{\rm sl}$, $P_{\rm sl}$, and $Q_{\rm sl}$ denote the point of common coupling (PCC) voltage, the reference of

Manuscript received June 3, 2017; revised October 27, 2017; accepted January 2, 2018. Date of publication January 17, 2018; date of current version September 28, 2018. This work was supported by the Hong Kong Research Grant Council under the theme-based project T23-701/14-N. Recommended for publication by Associate Editor F. W. Fuchs. *(Corresponding author: Ron Hui.)*

T. Yang, T. Liu, J. Chen, and S. Yan are with the Department of Electrical and Electronic Engineering, The University of Hong Kong, Hong Kong (e-mail: yang2014@connect.hku.hk; taoliu@eee.hku.hk; jiechen@eee.hku.hk; yanshuo@connect.hku.hk).

S.Y. Ron Hui is with the Department of Electrical and Electronic Engineering, The University of Hong Kong, Hong Kong and also with the Department of Electrical and Electronic Engineering, Imperial College London, London SW7 2AZ, U.K. (e-mail: ronhui@eee.hku.hk).

Color versions of one or more of the figures in this paper are available online at http://ieeexplore.ieee.org.

Digital Object Identifier 10.1109/TPEL.2018.2794516

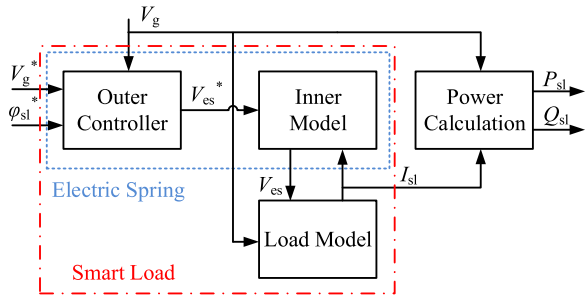

Fig. 1. System structure of the proposed model.

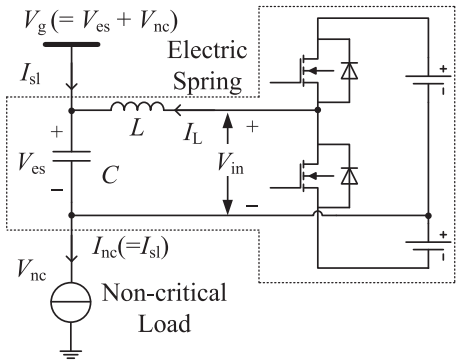

Fig. 2. Schematic of a smart load associated with ES-2.

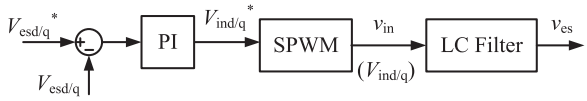

Fig. 3. Control scheme of ES using SPWM.

PCC voltage, the reference power angle of smart load, the ES voltage, the reference of ES voltage, the smart load current, the active power of smart load, and the reactive power of smart load. Section II introduces the inner model, which focuses on the hardware and core voltage-controlled dynamics of ES. The outer controller is illustrated with the radial-chordal decomposition (RCD) control strategy [11] in Section III. In Section IV, ZIP load model [19], [20] and thermostatic load model [21] commonly used in power system simulation are considered as the nonlinear noncritical loads for power grid analysis. Section V provides the model validation by comparing the experimental measurements with the model-predicted results. The proposed model is then demonstrated in 1) a power system based on an IEEE 13 nodes grid model [22] and 2) a three-phase microgrid system. Finally, the conclusion is given in Section VI.

The main contributions of this paper include the following.

1) A dynamic modular model of an ES-associated smart load in which the ES circuit, noncritical load, and controller can be modeled individually as separate modules and then integrated together.
2) An order-reduced model of an ES with reduced model complexity.
3) Incorporation of nonlinear loads into the ES-associated smart load model.

Compared with former analyses on modeling the behavior of ES [6], [16], [17], this paper presents an order-reduced dynamic model of ES with control loop in first time, and provides a novel modular modeling approach to ES-associated smart loads.

II. Inner Model

The characteristic of the electric circuit and the core voltage controller of ES (integrated as the inner model shown in the schematic of Fig. 1) is discussed in this section. The schematic of the smart load associated with the second version of ES (ES-2) is shown in Fig. 2 [8]. The ES can also be driven with a typical full bridge or some other specialized topologies [23]. The dc bus is supported by batteries or other voltage-controlled dc sources that allow bidirectional power flow. The noncritical load could typically be a water heater or other thermal loads that can tolerate some input voltage fluctuation. In Fig. 2, the noncritical load is represented as a current sink.

A few assumptions for the inner model are as follows.

1) Ideal switching devices and ideal *LC* filter components.
2) Ripples of output voltage of half-bridge (V_{in}) is neglected and so the dc bus voltage is assumed to be constant.
3) The delay introduced by the sensor and controller is neglected. In practice, a DSP controller (with 80 MHz clock and 20 kHz switching frequency) is implemented to generate the PWM signals.

The functional block of the voltage control loop of ES is shown in Fig. 3. Voltage and current signals will be decoupled into $d-q$ frame based on V_g. Proportional-integral (PI) controllers in $d-q$ frames together generate the voltage signal for sinusoidal PWM (SPWM) output.

A. Theoretical Model

From Fig. 2, the state equations of the filter components of ES can be expressed in the $d-q$ frame as follows:

$$\begin{cases} L{dI_{Ld}}/{dt} = I_{Lq}X_L - V_{\text{esd}} + V_{\text{ind}} \\ L{dI_{Lq}}/{dt} = -I_{Ld}X_L - V_{\text{esq}} + V_{\text{inq}} \\ C{dV_{\text{esd}}}/{dt} = I_{Ld} + \frac{1}{X_C}V_{\text{esq}} + I_{\text{sld}} \\ C{dV_{\text{esq}}}/{dt} = I_{Lq} - \frac{1}{X_C}V_{\text{esd}} + I_{\text{slq}} \end{cases} \tag{1}$$

where V_{es}, I_{sl}, I_L, X_L, and X_C stand for the ES voltage, smart load current, inductor current, the inductive reactance, and the capacitive reactance, respectively. The subscripts d and q refer to the d-axis and q-axis, respectively, in the $d-q$ frame. All the current and voltage variables are in r.m.s. values. For simplification, X_L and X_C are assumed to be constant. This assumption can be justified because frequency variation even in weak grids would not exceed the range of 48–52 Hz for a nominal frequency $f_0 = 50$ Hz.

The equations for the PI control loop are as follows:

$$\begin{cases} \frac{d\Phi_{\text{esd}}}{dt} = K_{id}\left({V_{\text{esd}}}^* - V_{\text{esd}}\right) \\ \frac{d\Phi_{\text{esq}}}{dt} = K_{iq}\left({V_{\text{esq}}}^* - V_{\text{esq}}\right) \\ V_{\text{ind}} = \Phi_{\text{esd}} + K_{pd}\left({V_{\text{esd}}}^* - V_{\text{esd}}\right) \\ V_{\text{inq}} = \Phi_{\text{esq}} + K_{pq}\left({V_{\text{esq}}}^* - V_{\text{esq}}\right) \end{cases} \tag{2}$$

where $V_{\rm es}^*$, $\Phi_{\rm es}$, K_p, and K_i stand for the reference ES voltage signal, integration of the errors (state variable of the PI controllers), proportional parameters, and integral parameters of the PI controller, respectively. The PI controllers for $d-q$ frame could be set individually. Note that the grid voltage (V_g) has real (d-axis) part only, as the local V_g sets the reference frame for each of the ES in common applications.

From (1) and (2), the state-space model equations are as follows:

$$\begin{cases} \dot{\boldsymbol{x}}_t = \boldsymbol{A}_t \boldsymbol{x}_t + \boldsymbol{B}_t \boldsymbol{u}_t \\ \boldsymbol{y}_t = \boldsymbol{C}_t \boldsymbol{x}_t \end{cases} \tag{3}$$

where $\boldsymbol{x}_t = [x_1\ x_2\ x_3\ x_4\ x_5\ x_6]^T$, $\boldsymbol{u}_t = [{V_{\rm esd}}^*\ {V_{\rm esq}}^*\ I_{\rm sld}\ I_{\rm slq}]^T$, $\boldsymbol{y}_t = [V_{\rm esd}\ \ V_{\rm esq}]^T$ with $x_1 = V_{\rm esd}$, $x_2 = V_{\rm esq}$, $x_3 = \Phi_{\rm esd}$, $x_4 = \Phi_{\rm esq}$, $x_5 = I_{Ld}$, $x_6 = I_{Lq}$ and

$$\boldsymbol{A}_t = \begin{bmatrix} 0 & \frac{1}{X_C C} & 0 & 0 & \frac{1}{C} & 0 \\ -\frac{1}{X_C C} & 0 & 0 & 0 & 0 & \frac{1}{C} \\ -K_{id} & 0 & 0 & 0 & 0 & 0 \\ 0 & -K_{iq} & 0 & 0 & 0 & 0 \\ -\frac{(K_{pd}+1)}{L} & 0 & \frac{1}{L} & 0 & 0 & 0 \\ 0 & -\frac{(K_{pq}+1)}{L} & 0 & \frac{1}{L} & 0 & 0 \end{bmatrix}$$

$$\boldsymbol{B}_t = \begin{bmatrix} 0 & 0 & \frac{1}{C} & 0 \\ 0 & 0 & 0 & \frac{1}{C} \\ K_{id} & 0 & 0 & 0 \\ 0 & K_{iq} & 0 & 0 \\ \frac{K_{pd}}{L} & 0 & 0 & 0 \\ 0 & \frac{K_{pq}}{L} & 0 & 0 \end{bmatrix},\ \boldsymbol{C}_t = \begin{bmatrix} 1 & 0 & 0 & 0 & 0 & 0 \\ 0 & 1 & 0 & 0 & 0 & 0 \end{bmatrix}.$$

The characteristic polynomial of $\boldsymbol{A}_t$ is described as follows:

$$\begin{aligned} a(z) &= \det(z\boldsymbol{I} - \boldsymbol{A}_t) \\ &= z^6 + \frac{z^4\left(2LC + K_{pd}LC + K_{pq}LC + {X_L}/{X_C}\right)}{L^2C^2} \\ &+ \frac{z^3(K_{id}LC + K_{iq}LC)}{L^2C^2} + \frac{z^2(1 + K_{pd} + K_{pq} + K_{pd}K_{pq})}{L^2C^2}. \\ &+ \frac{z(1 + K_{id} + K_{iq} + K_{id}K_{pq} + K_{pd}K_{iq})}{L^2C^2} + \frac{K_{id}K_{iq}}{L^2C^2} \end{aligned} \tag{4}$$

The eigenvalues of $\boldsymbol{A}_t$, denoted as $\lambda_i(\boldsymbol{A}_t)$, where $i = 1, 2, \ldots, 6$, are roots of (4) and reflect the poles of the system. With experimental parameters provided, the eigenvalues can be obtained and will be used for further analysis.

The controllability of such a continuous linear time-invariant state-space model is determined by $(\boldsymbol{A},\ B)$. The controllability matrix $\boldsymbol{M}$ could be described as follows:

$$\begin{aligned} \boldsymbol{M} &= \left[\boldsymbol{B}_t\ \boldsymbol{A}_t\boldsymbol{B}_t\ \cdots\ {\boldsymbol{A}_t}^5\boldsymbol{B}_t\right] = \left[\boldsymbol{B}_t\ \boldsymbol{A}_t\boldsymbol{B}_t \mid *\right] \\ &= \left[\boldsymbol{M}_1 \mid *\right] \end{aligned} \tag{5}$$

TABLE I
SINGLE SMART LOAD TEST PARAMETERS

$V_{\rm g}$	f_0	L	C	R	K_{pd}	K_{id}	K_{pq}	K_{iq}
110 V	50 Hz	0.6 mH	4.7 μF	40 Ω	0.1	25	0.1	25

where

$$\boldsymbol{M}_1 = \begin{bmatrix} 0 & 0 & \frac{1}{C} & 0 & \frac{K_{pd}}{LC} & 0 & 0 & \frac{1}{X_C C^2} \\ 0 & 0 & 0 & \frac{1}{C} & 0 & \frac{K_{pq}}{LC} & -\frac{1}{X_C C^2} & 0 \\ K_{id} & 0 & 0 & 0 & 0 & 0 & -\frac{K_{id}}{C} & 0 \\ 0 & K_{iq} & 0 & 0 & 0 & 0 & 0 & -\frac{K_{iq}}{C} \\ \frac{K_{pd}}{L} & 0 & 0 & 0 & \frac{K_{id}}{L} & 0 & -\frac{(K_{pq}+1)}{LC} & 0 \\ 0 & \frac{K_{pq}}{L} & 0 & 0 & 0 & \frac{K_{iq}}{L} & 0 & -\frac{(K_{pd}+1)}{LC} \end{bmatrix}.$$

When $K_{id/q}$ and $K_{pd/q}$ are positive (Note: This is a sufficient condition only), it can be shown that $|\boldsymbol{M}_1{\boldsymbol{M}_1}^T| > 0$. Therefore, $\boldsymbol{M}_1$ has a full row rank and then the system is controllable.

In such a model, the ES is regarded as a multiple-input and multiple-output system. Specifically, the ES voltage reference $(V_{\rm es}^*)$ and smart load current $(I_{\rm sl})$ in $d-q$ frame are the inputs, while the ES voltage $(V_{\rm es})$ in $d-q$ frame are the outputs. Although $V_{\rm es}^*$ and $I_{\rm sl}$ are both input signals in the model, $I_{\rm sl}$ is not independently controlled but determined by the nature of the system automatically.

B. Estimated Model

For complex simulation setups, such as in a microgrid equipped with multiple smart loads associated with ES, an accurate and low-order model is highly desired. The theoretical state-space model in the previous section has an order of 6, implying that simulation of a group of ES in a power system environment will be complex and time-consuming. Moreover, as the high-order performance may not contribute much to the interested dynamic performance, such a complex smart-load model may be unnecessary. To obtain an accurate order-reduced model that focuses on the main contribution of the smart load, the method of slow-fast decomposition [24], [25] can be utilized.

According to the modal decomposition theory [26], a state equation can be expressed as a linear combination of the various modes. Considering the slow-fast decomposition, the state-space model can be described as follows:

$$\boldsymbol{G}_t(s) = \boldsymbol{G}_{\rm slow}(s) + \boldsymbol{G}_{\rm fast}(s) \tag{6}$$

where $\boldsymbol{G}_t(s) = \left[\frac{\boldsymbol{A}_t \mid \boldsymbol{B}_t}{\boldsymbol{C}_t \mid 0}\right]$, $\boldsymbol{G}_{\rm slow}(s) = \left[\frac{\tilde{\boldsymbol{A}}_s \mid \tilde{\boldsymbol{B}}_s}{\tilde{\boldsymbol{C}}_s \mid 0}\right]$, and $\boldsymbol{G}_{\rm fast}(s) = \left[\frac{\tilde{\boldsymbol{A}}_f \mid \tilde{\boldsymbol{B}}_f}{\tilde{\boldsymbol{C}}_f \mid 0}\right]$ denote the original theoretical model, the decomposed slow portion, and the fast portion, respectively.

By eigenvalue analysis, the eigenvalues with smaller modulus reflect the poles of the slow portion, while the eigenvalues with larger modulus reflect the poles of the fast portion. By substituting the practical parameters in Table I into the model, the

eigenvalues of the theoretical model can be obtained as follows:

$$\boldsymbol{E}_t = \begin{bmatrix} \lambda_1 & \lambda_2 & \lambda_3 & \lambda_4 & \lambda_5 & \lambda_6 \end{bmatrix} \tag{7}$$

with $\lambda_1 = -22.73 + j0.000416$, $\lambda_2 = -22.73 - j0.000416$, $\lambda_3 = 11.45 - j19590$, $\lambda_4 = 11.45 + j19590$, $\lambda_5 = 11.27 + j19910$, and $\lambda_6 = 11.27 - j19910$.

Here, we decompose the theoretical model into slow and fast portions by a specific cut-off frequency f_c to illustrate how the inputs impact the models' response. This f_c is set at 1 kHz, i.e., 20 times of the grid frequency. Considering the switching frequency of the inverter is 20 kHz and the associated low-pass filter has a predesigned cut-off frequency at 3 kHz, it is reasonable to assume that the frequency lower than f_c contributes most of the dynamics of the ES. According to (7), λ_1 and λ_2 contribute to the slow portion and the other eigenvalues contribute to the fast portion.

By using Real Schur decomposition [27], for the square matrix $\boldsymbol{A}_t$, one can always find an orthogonal matrix $\boldsymbol{V}$ that

$$\tilde{\boldsymbol{A}} = \boldsymbol{V}\boldsymbol{A}_t\boldsymbol{V}^T = \begin{bmatrix} \tilde{\boldsymbol{A}}_s & \tilde{\boldsymbol{A}}_{12} \\ 0 & \tilde{\boldsymbol{A}}_f \end{bmatrix}. \tag{8}$$

To remove $\tilde{\boldsymbol{A}}_{12}$ by similarity transformations, we can find a solution $\boldsymbol{X}$ for a Sylvester equation

$$\tilde{\boldsymbol{A}}_s\boldsymbol{X} - \boldsymbol{X}\tilde{\boldsymbol{A}}_f + \tilde{\boldsymbol{A}}_{12} = 0. \tag{9}$$

Additionally, we have the following:

$$\begin{cases} \begin{bmatrix} \tilde{\boldsymbol{B}}_s \\ \tilde{\boldsymbol{B}}_f \end{bmatrix} = \left(\begin{bmatrix} \boldsymbol{I} & -\boldsymbol{X} \\ 0 & \boldsymbol{I} \end{bmatrix} \boldsymbol{V} \right) \boldsymbol{B}_t = \boldsymbol{P}\boldsymbol{B}_t, \\ \begin{bmatrix} \tilde{\boldsymbol{C}}_s & | & \tilde{\boldsymbol{C}}_f \end{bmatrix} = \boldsymbol{C}_t \left(\boldsymbol{V}^T \begin{bmatrix} \boldsymbol{I} & \boldsymbol{X} \\ 0 & \boldsymbol{I} \end{bmatrix} \right) = \boldsymbol{C}_t\boldsymbol{P}^{-1} \end{cases} \tag{10}$$

where $\boldsymbol{P}$ denotes the similarity matrix.

The slow–fast decomposed models are finally achieved. Note that such slow–fast decomposition is based on eigenvalues of the state matrix and numerically solving of the Sylvester equation, it can be computed by various means, e.g., MATLAB *slowfast* or *freqsep* commands, but only be obtained in numeric. The results of the decomposition are shown as the following equations:

$$\begin{cases} \dot{\boldsymbol{x}}_s = \tilde{\boldsymbol{A}}_s\boldsymbol{x}_s + \begin{bmatrix} \tilde{\boldsymbol{B}}_s & | & \tilde{\boldsymbol{B}}_{s'} \end{bmatrix} \boldsymbol{u}_t \\ \boldsymbol{y}_s = \tilde{\boldsymbol{C}}_s\boldsymbol{x}_s \end{cases} \tag{11}$$

where $\boldsymbol{x}_s = [\, x_{s1}\ x_{s2} \,]^T$, $\boldsymbol{u}_t = [\, {V_{\rm esd}}^*\ {V_{\rm esq}}^*\ I_{\rm sld}\ I_{\rm slq} \,]^T$, $\boldsymbol{y}_s = [\, V_{\rm esds}\ V_{\rm esqs} \,]^T$ ($V_{\rm esds}$ and $V_{\rm esqs}$ denote the slow portion of outputs) with $\tilde{\boldsymbol{A}}_s = \begin{bmatrix} -22.73 & -0.000416 \\ 0.000416 & -22.73 \end{bmatrix}$, $\tilde{\boldsymbol{B}}_s = \begin{bmatrix} 0.9844 & -1.025 \\ -1.025 & -0.9844 \end{bmatrix}$, $\tilde{\boldsymbol{B}}_{s'} = \begin{bmatrix} 0.01342 & -0.01398 \\ -0.01398 & -0.01342 \end{bmatrix}$, and $\tilde{\boldsymbol{C}}_s = \begin{bmatrix} 10.07 & -10.49 \\ -10.49 & -10.07 \end{bmatrix}$.

$$\begin{cases} \dot{\boldsymbol{x}}_f = \tilde{\boldsymbol{A}}_f\boldsymbol{x}_f + \tilde{\boldsymbol{B}}_f\boldsymbol{u}_t \\ \boldsymbol{y}_f = \tilde{\boldsymbol{C}}_f\boldsymbol{x}_f \end{cases} \tag{12}$$

where $\boldsymbol{x}_f = [x_{f1}\ x_{f2}\ x_{f3}\ x_{f4}]^T$, $\boldsymbol{u}_t = [{V_{\rm esd}}^*\ {V_{\rm esq}}^*\ I_{\rm sld}\ I_{\rm slq}]^T$, $\boldsymbol{y}_f = [\, V_{\rm esdf}\ V_{\rm esqf} \,]^T$ ($V_{\rm esdf}$ and $V_{\rm esqf}$ denote the fast portion of outputs) with

$$\tilde{\boldsymbol{A}}_f = \begin{bmatrix} 11.27 & 19910 & -9.904 & 11910 \\ -19910 & 11.27 & 11910 & 9.904 \\ 0 & 0 & 11.45 & 19590 \\ 0 & 0 & -19590 & 11.45 \end{bmatrix},$$

$$\tilde{\boldsymbol{B}}_f = \begin{bmatrix} -0.05733 & -1.544 & 344.4 & -4.551 \\ 1.544 & -0.05733 & 4.551 & 344.4 \\ -0.002923 & 2.096 & 246.4 & -2.657 \\ 2.096 & 0.002923 & -2.657 & -246.4 \end{bmatrix},$$

and

$$\tilde{\boldsymbol{C}}_f = \begin{bmatrix} 412.3 & 6.083 & 303.9 & -2.637 \\ -6.083 & 412.3 & -2.637 & -303.9 \end{bmatrix}.$$

As shown in Figs. 2 and 3, the inner model of the ES itself could be regarded as a voltage-controlled device, so V_{es}^* will naturally be the input signal in the new model. If $I_{\rm sl}$ (as a disturbance input) can be ignored, a further simplified model can be achieved. We further notice that the elements of the submatrix $[\, P_{11}\ P_{12}\ ;\ P_{21}\ P_{22} \,]$ in $\boldsymbol{P}$ are extremely small with a magnitude of $10^{-7\sim-6}$. Therefore, as shown in the input matrix of (11), the absolute values of the elements in $\tilde{\boldsymbol{B}}_s$ are considerably larger than the ones in $\tilde{\boldsymbol{B}}_{s'}$, i.e., the absolute values in $\tilde{\boldsymbol{B}}_s$ is higher than the ones in $\tilde{\boldsymbol{B}}_{s'}$ by two orders of magnitude. Hence, in the model of slow components $\boldsymbol{G}_{\rm slow}(s)$, the output results are dominated by the control signals of voltage $V_{{\rm esd}/q}^*$, which is desired as a voltage-controlled inverter. The current signals $I_{{\rm sld}/q}$ thus are ignored to further simplify the model in the following section. To be noted, such simplification is parameter-based. If the specification of the ES is changed, the decomposition must be checked to guarantee a valid simplification. Fig. 4 shows the output comparison among the originally theoretical model ($V_{{\rm esd}/q}$), slow ($V_{{\rm esd}/qs}$) and fast ($V_{esd/qf}$) components with a same step-change input. The dynamic response of the theoretical model is fine for the anticipated operation of an ES [6], [7]. According to the results shown in Fig. 4, it is clear that the slow components $\boldsymbol{G}_{\rm slow}(s)$, which are of second order, contribute to the major portions of the dynamic and static behaviors of the outputs. As a result, the structure of the model focusing on the voltage performance could be described as follows:

$$\begin{cases} \dot{\mathbf{x}}_{\rm e} = \mathbf{A}_{\rm e}\mathbf{x}_{\rm e} + \mathbf{B}_{\rm e}\mathbf{u}_{\rm e} \\ \mathbf{y}_{\rm e} = \mathbf{C}_{\rm e}\mathbf{x}_{\rm e} \end{cases} \tag{13}$$

where $\mathbf{x}_{\rm e} = [\, x_{\rm e1}\ x_{\rm e2} \,]^T$, $\mathbf{u}_{\rm e} = [\, {V_{\rm esd}}^*\ {V_{\rm esq}}^* \,]^T$, and $\mathbf{y}_{\rm e} = [\, \hat{V}_{\rm esd}\ \hat{V}_{\rm esq} \,]^T$ ($\hat{V}_{\rm esd}$ and $\hat{V}_{\rm esq}$ denote the model-predicted outputs).

A nonlinear model is not preferred in this case, as it increases the complexity of the model and computational burden in the simulation process, which is against the original intention. To make the estimation process as simple as possible, the commonly used prediction error methods (PEM) with Gauss–Newton algorithm are chosen from a family of estimation methods for parameter estimation. The limitation of the estimated model is that it requires re-estimation if the key components or the inner model parameters of the ES have changed. The estimation and its results will be discussed in Phase I of Section V.

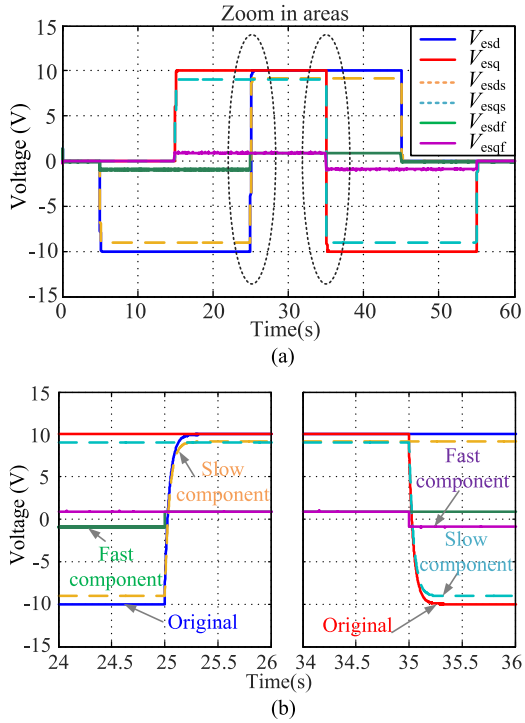

Fig. 4. Outputs of $\boldsymbol{G}_t(s)$, $\boldsymbol{G}_{\text{slow}}(s)$, and $\boldsymbol{G}_{\text{fast}}(s)$ components base on the theoretical model. (a) Full results of $\boldsymbol{G}_t(s)$, $\boldsymbol{G}_{\text{slow}}(s)$, and $\boldsymbol{G}_{\text{fast}}(s)$ components. (b) Zoom in results of $\boldsymbol{G}_t(s)$, $\boldsymbol{G}_{\text{slow}}(s)$, and $\boldsymbol{G}_{\text{fast}}(s)$ components.

III. Outer Controller

In order to achieve various control method for grid interaction, this module of outer controller generates the voltage reference for the ES, as shown in Fig. 1. Compared with the voltage controller included in the inner model, which is usually preset in the hardware design phase, the outer controller is prepared to achieve superior control objective. Based on the inner model achieved, the smart load model can represent accurate and credible results driven by the outer controller's signal. For demonstration, the RCD control is adopted for instance to mitigate the voltage fluctuation by adjusting active/reactive power of the smart load with ES embedded. Compared with other control methods [8]–[10], RCD control can effectively adjust the power of the smart load while maintaining the noncritical load voltage in a preferred range during operation. Moreover, RCD control can regulate the power factor of the smart load independently. As shown in Fig. 5, with "O" as the center of a circle, V_{es} can be decomposed into V_{esr} (radial part) and V_{esc} (chordal part), which determine the voltage of the noncritical load (V_{nc}) and the power angle of the smart load (φ_{sl}) respectively and independently. And φ_{nc}, θ_o, and θ_{esr} denote the power angle of the noncritical load, the angle between V_{nc} and V_g, and the angle between V_{esr} and V_g, respectively (as V_{esr} is in phase of V_{nc}, $\theta_o = \theta_{\text{esr}}$). When RCD control is applied in a weak microgrid, V_{esr} will be used to dynamically compensate the voltage fluctuation, and V_{esc} is calculated based on the power factor reference signal from an imaginary control center to adjust the active and reactive power consumption. The outer controller scheme is shown in Fig. 6.

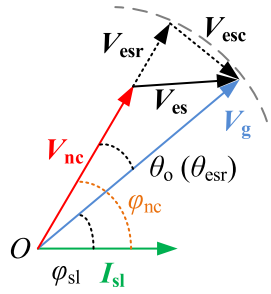

Fig. 5. Arbitrary sketch of the voltage and current phasors in RCD control.

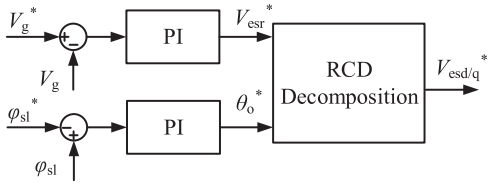

Fig. 6. Outer controller scheme based on RCD control.

In Fig. 6, ${\varphi_{\text{sl}}}^*$ stands for reference of the smart load's power angle. Since the voltage sensed at PCC (V_g) is set as the common reference frame for the $d-q$ frame transformation in each ES system, the instantaneous power angle of smart load is as follows:

$$\varphi_{\text{sl}} = -\text{atan}\left(\frac{I_{\text{slq}}}{I_{\text{sld}}}\right), \varphi_{\text{sl}} \in [-\pi, \pi]. \tag{14}$$

Following the phasor relationship shown in Fig. 5, the reference phasor based on PCC voltage and power angle are derived as follows:

$$\begin{cases} \sqrt{2}{V_{\text{esr}}}^* \angle {\theta_{\text{esr}}}^* = \sqrt{2}{V_{\text{esr}}}^* \angle {\theta_{\text{o}}}^* \\ \sqrt{2}{V_{\text{esc}}}^* \angle {\theta_{\text{esc}}}^* = \sqrt{2}V_{\text{g}}\sqrt{2\left(1-\cos{\theta_{\text{o}}}^*\right)} \angle \frac{{\theta_{\text{o}}}^* - \text{sign}({\theta_{\text{o}}}^*)\pi}{2} \end{cases} \tag{15}$$

where $\text{sign}(x) = \begin{cases} 1, & \text{when } x > 0 \\ -1, & \text{when } x \le 0 \end{cases}$, and ${V_{\text{esc}}}^*$ is derived from the trigonometric identities on the triangle composed with V_{nc}, V_{esr}, V_{esc}, and V_g.

Based on (15), the algebraic equations of the control scheme with PI controllers in Fig. 6 can be further derived as follows:

$$\begin{cases} {V_{\text{esr}}}^* = K_{\text{p1}}\left(V_{\text{g}}^* - V_{\text{g}}\right) + K_{\text{i1}}\int\left(V_{\text{g}}^* - V_{\text{g}}\right) \\ {\theta_{\text{esr}}}^* = {\theta_{\text{o}}}^* = K_{\text{p2}}\left(\varphi_{\text{sl}} - {\varphi_{\text{sl}}}^*\right) + K_{\text{i2}}\int\left(\varphi_{\text{sl}} - {\varphi_{\text{sl}}}^*\right) \\ {V_{\text{esc}}}^* = V_{\text{g}}\sqrt{2\left(1-\cos{\theta_{\text{o}}}^*\right)} \\ {\theta_{\text{esc}}}^* = \frac{{\theta_{\text{o}}}^* - \text{sign}({\theta_{\text{o}}}^*)\pi}{2} \end{cases} \tag{16}$$

where $K_{p/i1}$ and $K_{p/i2}$ denote the PI controller parameters for V_{esr}^* control and θ_o^* control.

To combine with the inner model in the $d-q$ frame, the voltage reference of RCD control could be decoupled into $d-q$ frame as (17). Otherwise, it can be rearranged into time domain

sinusoidal form as (18)

$$\begin{cases} {V_{\rm esd}}^* = {V_{\rm esr}}^* \cos {\theta_{\rm o}}^* + {V_{\rm esc}}^* \cos\left(\frac{{\theta_{\rm o}}^* - {\rm sign}({\theta_{\rm o}}^*)\pi}{2}\right) \\ {V_{\rm esq}}^* = {V_{\rm esr}}^* \sin {\theta_{\rm o}}^* + {V_{\rm esc}}^* \sin\left(\frac{{\theta_{\rm o}}^* - {\rm sign}({\theta_{\rm o}}^*)\pi}{2}\right) \end{cases} \quad (17)$$

$$v_{\rm es} = \sqrt{2}{V_{\rm esr}}^* \cos\left(\omega t + {\theta_{\rm o}}^*\right) + \sqrt{2}{V_{\rm esr}}^* \cos\left(\omega t + \frac{{\theta_{\rm o}}^* - {\rm sign}({\theta_{\rm o}}^*)\pi}{2}\right). \quad (18)$$

With the voltage and current information of the ES, the active/reactive power exchanged via ES, $P_{\rm es}$ and $Q_{\rm es}$, can be calculated in the $d-q$ frame as follows:

$$\begin{cases} P_{\rm es} = V_{\rm esd} I_{\rm sld} + V_{\rm esq} I_{\rm slq} \\ Q_{\rm es} = V_{\rm esq} I_{\rm sld} - V_{\rm esd} I_{\rm slq} \end{cases}. \quad (19)$$

Although an ideal constant dc bus is assumed in this model and the active power exchanged via ES is relatively small compared with the whole smart load power consumption [8], the active/reactive power of ES should be considered in practical hardware and outer controller design (e.g., for batteries management). Similar to (19), the active/reactive power of the smart load can be calculated by the sensed V_g and $I_{\rm sl}$, which refer to the power calculation block in Fig. 1.

IV. Load Model

In this section, the module of load model as shown in Fig. 1 is analyzed and discussed. In previous studies of ES, a fixed impedance (mostly resistor) is usually chosen as the noncritical load. To broaden the application range of the proposed model, a ZIP load model and a thermostatic load model (well known in power system studies [21]) are adopted in this section as nonlinear static and dynamic electric loads, respectively.

A. ZIP Load Model

A ZIP load model represents the load power, which comprises power consumed by constant impedance (*Z*), current (*I*), and power (*P*) components, described as follows:

$$P = P_0 \left[Z_p \left(\frac{V}{V_0}\right)^2 + I_p \left(\frac{V}{V_0}\right) + P_p \right] \quad (20)$$

where P_0 is the active power consumed by the load at the rated voltage V_0, V is the actual load voltage, Z_p, I_p, and P_p are the coefficients for the constant impedance, current, and power respectively. In this paper, the ZIP consumes active power only (i.e., its reactive power consumption is zero). While the ZIP load is a voltage-dependent and pure resistive equivalent load, it should be noted from Fig. 5 that the ES could provide reactive power compensation to the overall smart load (comprising the ES and the ZIP load in this case). So the load model also involves current variables in the $d-q$ frame based on PCC voltage V_g.

To link such a load characteristic with the proposed inner model, the load is represented as a current sink. For each single smart load with the PCC voltage, the constant impedance part can be described as follows:

$$\begin{cases} I_{zd} = \dfrac{V_g - V_{\rm esd}}{R} \\ I_{zq} = \dfrac{-V_{\rm esq}}{R} \end{cases} \quad (21)$$

where R is the equivalent resistor of the constant impedance part and $R = {V_0}^2/(P_0 Z_0)$.

For the constant current part, the apparent power of the noncritical load, S, can be expressed as follows:

$$\begin{aligned} S &= V_{\rm nc} \bar{I}_i \\ &= \left[\left(V_g - V_{\rm esd}\right) I_{id} - V_{\rm esq} I_{iq}\right] - j\left[V_{\rm esq} I_{id} + \left(V_g - V_{\rm esd}\right) I_{iq}\right] \\ &= P_i - j0. \end{aligned} \quad (22)$$

As the current r.m.s. value is constant, we have the following:

$$\begin{cases} I_{id}^2 + I_{iq}^2 = I_{\rm const}^2 \\ V_{\rm esq} I_{id} + \left(V_g - V_{\rm esd}\right) I_{iq} = 0 \end{cases} \Rightarrow \begin{cases} I_{id} = I_{\rm const} \frac{V_g - V_{\rm esd}}{V_g - V_{\rm esr}} \\ I_{iq} = I_{\rm const} \frac{-V_{\rm esq}}{V_g - V_{\rm esr}} \end{cases}. \quad (23)$$

For the constant power part, similarly, we have the following:

$$\begin{aligned} S &= V_{\rm nc} \bar{I}_p \\ &= \left[\left(V_g - V_{\rm esd}\right) I_{pd} - V_{\rm esq} I_{pq}\right] - j\left[V_{\rm esq} I_{pd} + \left(V_g - V_{\rm esd}\right) I_{pq}\right] \\ &= P_{\rm const} - j0. \end{aligned} \quad (24)$$

The relationship of the equivalent current source can be derived as follows:

$$\begin{cases} \left(V_g - V_{\rm esd}\right) I_{pd} - V_{\rm esq} I_{pq} = P_{\rm const} \\ V_{\rm esq} I_{pd} + \left(V_g - V_{\rm esd}\right) I_{pq} = 0 \end{cases} \Rightarrow \begin{cases} I_{pd} = P_{\rm const} \frac{V_g - V_{\rm esd}}{\left(V_g - V_{\rm esr}\right)^2} \\ I_{pq} = P_{\rm const} \frac{-V_{\rm esq}}{\left(V_g - V_{\rm esr}\right)^2} \end{cases}. \quad (25)$$

In conclusion, the total equivalent current source model of the noncritical load in ZIP form can be expressed as follows:

$$\begin{cases} I_{\rm sld} = \frac{V_g - V_{\rm esd}}{R} + I_{\rm const} \frac{V_g - V_{\rm esd}}{V_g - V_{\rm esr}} + P_{\rm const} \frac{V_g - V_{\rm esd}}{\left(V_g - V_{\rm esr}\right)^2} \\ I_{\rm slq} = \frac{-V_{\rm esq}}{R} + I_{\rm const} \frac{-V_{\rm esq}}{V_g - V_{\rm esr}} + P_{\rm const} \frac{-V_{\rm esq}}{\left(V_g - V_{\rm esr}\right)^2} \end{cases}. \quad (26)$$

B. Thermostatic Load Model

If the dynamic responses of the electric loads are needed in a power system study, a dynamic thermostatic load model described in [21] can be used. A suitable thermostatic load could be a water heater, as it is insensitive with voltage fluctuation and has large thermal inertia as a noncritical load. Fig. 7 shows a dynamic model for the thermostatically controlled loads, where

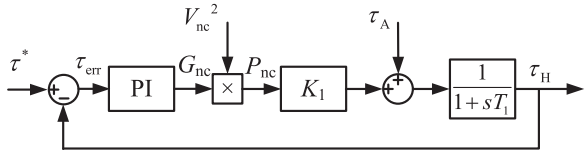

Fig. 7. Commonly used model for thermostatically controlled loads.

τ^*, τ_A, and τ_H stand for the reference temperature, the ambient area temperature, and the controlled area temperature, respectively. The temperature error $(\tau_{\rm err})$ is the input for the PI controller. The PI controller's effort is to regulate the load conductance $(G_{\rm nc})$ within a preset range $[0,\, G_{\max}]$. As the device consumes pure active power only, the power consumed by the load $(P_{\rm nc})$ could be represented as the product of the $G_{\rm nc}$ and the square of the device voltage $(V_{\rm nc}^2)$. K_1 represents a gain associated with the load model, indicating the transformation from the power to the device temperature. Finally, there is a first-order transfer function representing heat transfer from the device body to the temperature controlled area, based on the thermal time constant T_1.

Assuming the load is a heating device, the dynamic equation representing the temperature could be expressed as follows:

$$\frac{d\tau_H}{dt} = \frac{K_1}{T_1} G_{\rm nc} {V_{\rm nc}}^2 + \frac{1}{T_1}\left(\tau_A - \tau_H\right). \tag{27}$$

The PI controller and the first-order transfer function are represented as $C_{\rm PI}$ and C_1, respectively. From Fig. 7, $G_{\rm nc}$ can be described as follows:

$$G_{\rm nc} = \frac{\left(\tau^* - C_1\tau_A\right) C_{\rm PI}}{1 + C_1 C_{PI} K_1 (V_g - V_{\rm esr})^2}. \tag{28}$$

Similar to the analysis of the ZIP load, when the load conductance is obtained, the equivalent currents of the thermostatic load model are as follows:

$$\begin{cases} I_{\rm sld} = \left(V_g - V_{\rm esd}\right) G_{\rm nc} \\ I_{\rm slq} = -V_{\rm esq} G_{\rm nc} \end{cases}. \tag{29}$$

Hence, both the ZIP load and the thermostatic load models are ready to combine with the proposed model.

V. Experiment and Simulation Results

In this section, the practical voltage response of the ES prototype is first measured. The experimental data are used for estimating the model parameters. Second, experiments and simulations are conducted on a smart load (associated with ES), which is fed by a stiff single-phase power source. Measurements are used for comparison between the theoretical and the estimated model. Third, a single-phase micro power system installing three smart loads is set up to further validate the model. Then, an IEEE 13 Node test feeder with multiple smart loads is set up in Simulink to demonstrate the effectiveness of the proposed model in simulation. Finally, a demonstration for voltage and frequency compensation using a single smart load with ES is conducted. In all the simulations, the dc link of the ES is assumed to be ideal. In the simulation containing multiple smart loads (Phase III and Phase IV) with ES associated, a control center is assumed and the control signal transmission delay is ignored.

A. Phase I

To obtain experimental data for estimation, a smart load with ES is set up as shown in Fig. 8. The smart load with ES is connected to a stiff single-phase ac source. The ES is controlled

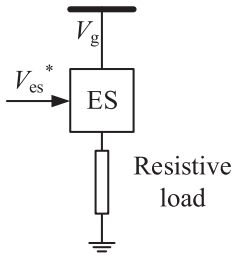

Fig. 8. System setup in phase I.

directly by preset voltage reference $V_{\rm es}^*$. The outer controller is omitted as there is no interaction with the grid in this phase. A constant resistive load is used as the noncritical load. A 20 kHz PWM half-bridge power inverter is used to develop the ES, which is powered by a 120 V bidirectional dc supply. The inner voltage control is implemented in a dSPACE control platform. The units of the sensed signals have been normalized due to the implicit amplification in all sensors and ADC transformation processes. The parameters of the ac voltage (V_g), ac frequency (ω), *LC* filter $(L,\, C)$, noncritical load (*R*), and PI controllers $(K_{pd/q},\, K_{id/q})$ are tabulated in Table I as mentioned previously.

In the experiment with a period of 60 s, $V_{\rm es}^*$ is set to 0 for initialization during the period from $t = 0\,$s to $t = 5\,$s. At $t = 5\,$s, $t = 25\,$s, and $t = 45\,$s, $V_{\rm esd}^*$ step-changes to -10, 10, and 0 V, respectively. At $t = 15\,$s, $t = 35\,$s, and $t = 55\,$s, $V_{\rm esq}^*$ step-changes to 10, -10, and 0 V, respectively. The ES voltage responses under the corresponding references are shown in Fig. 9(a) and (b) (labeled $V_{\rm esd/qExp}$). Such responses are collected in time series as $Z^N = \{u(1), y(1), u(2), y(2), \ldots u(N), y(N)\}$, where u and y denote the input and output of the ES, N denotes the number of sample in the period.

One can use Z^N to estimate the model parameters with various system identification methods, such as PEM, maximum likelihood method, and subspace method [28]. In this paper, the PEM is adopted due to its wide spectrum of model parameterizations and excellent asymptotic properties. By using PEM, the model can be described as a predictor of the next output with a finite dimensional parameter vector γ:

$$y_e\left(t \mid \gamma\right) = f\left(Z^{t-1}, \gamma\right) \tag{30}$$

where $f(.)$ is an arbitrary function of the past collected data, and $y_e(t \mid \gamma)$ denotes the one-step ahead prediction of the output. With $f(.)$ defined as (13), and Z^N collected, the estimation of parameter vector γ is to minimize the distance between the predicted output and the measurements

$$\begin{cases} \hat{\gamma}_N = \arg\min\limits_{\gamma} V_N\left(\gamma\right) \\ V_N\left(\gamma\right) = \frac{1}{N}\sum\limits_{t=1}^{N} \ell\left(y\left(t\right) - f\left(Z^{t-1}, \gamma\right)\right) \end{cases} \tag{31}$$

where $\ell(.)$ is a selected distance measure, such as $\ell(\varepsilon) = \|\varepsilon\|^2$. In general, (30) cannot be solved by analytical methods. The solution has to be found by iterative numerical techniques. Typical numerical search methods for iterative parameter estimation methods include Gauss–Newton methods, steepest descent

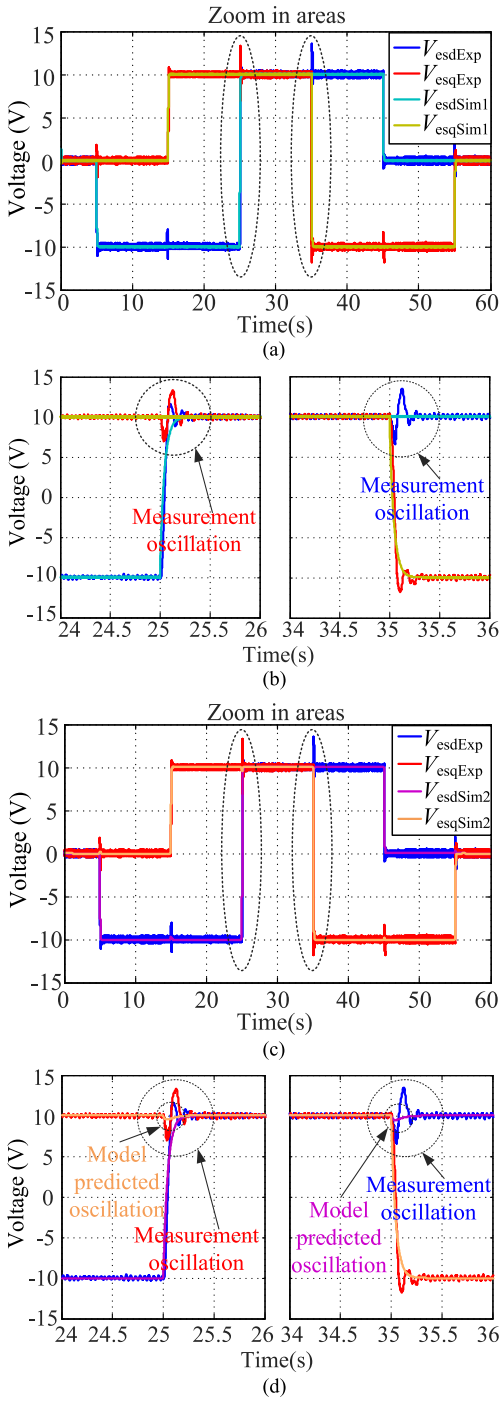

Fig. 9. Experimental and simulation (theoretical and estimated models) results of ES output voltage. (a) Full results of experiment and the theoretical model. (b) Zoom in results of experiment and the theoretical model. (c) Full results of experiment and the estimated model. (d) Zoom in results of experiment and the estimated model.

least-squares methods, and damped least-squares method (also known as Levenberg–Marquardt algorithm), and so on. The plenty of numerical search methods for iterative parameter estimation and their actual calculation could be a complicated story, which is beyond this paper.

By adopting subspace Gauss–Newton method provided in MATLAB for iterative parameter estimation, a model in form of (13) is estimated after ten iterations (there is no need for further calculation, as the improvements are extremely limited after ten iterations) [29]. The final estimated model is formed in observable canonical form shown as follows:

$$\begin{cases} \dot{\boldsymbol{x}}_e = \begin{bmatrix} -22.84 & -1.67 \\ 1.455 & -22.46 \end{bmatrix} \boldsymbol{x}_e + \begin{bmatrix} 22.87 & 1.671 \\ -1.441 & 22.49 \end{bmatrix} \boldsymbol{u}_e \\ \boldsymbol{y}_e = \begin{bmatrix} 1 & 0 \\ 0 & 1 \end{bmatrix} \boldsymbol{x}_e \end{cases} \tag{32}$$

where $\boldsymbol{x}_e = [\,x_{e1} \quad x_{e2}\,]^T$, $\boldsymbol{u}_e = [\,V_{\rm esd}{}^* \quad V_{\rm esq}{}^*\,]^T$, $\boldsymbol{y}_e = [\,\hat{V}_{\rm esd} \quad \hat{V}_{\rm esq}\,]^T$.

With a final prediction error of 0.0102 and a mean square error (MSE) of 0.202, the two sets of outputs of the estimated model fit the observation very well by achieving goodness-of-fit (evaluated by the normalized root mean square error) of 96.09% and 96.12%, respectively. Fig. 9 shows the experimental measurements (labeled $V_{\rm esd/qExp}$) and the responses of both the theoretical (labeled $V_{esd/qSim1}$) and the estimated (labeled $V_{esd/qSim2}$) model. In the zoom-in view as Fig. 9(b) and (d), it is observed that the responses of all the three curves are overlapped not only in the static state, but also in the rising and falling transient processes. The only relatively distinct difference among the curves is the oscillation, which occurs in the sudden change of the references. For the theoretical model, such oscillation is nearly invisible. For the estimated model, the oscillation is visible but much smoother than the one from the experimental measurement. Such oscillation in experiment may be triggered by transient energy exchange between the ES and the dc supply. In practice, sudden changes on the phase and amplitude of sinusoidal wave result in transient energy imbalance, such energy imbalance could cause voltage oscillation and hence influences the Fourier transformed results in the $d-q$ frame significantly. As the dc supply is ideal in the theoretical model, such phenomenon is not predicted. On the other hand, although the estimated model is based on the measurement, such oscillation is beyond the interested frequency band. Therefore, the order-reduced model only predicts smooth oscillation. Nevertheless, considering the small magnitude of oscillation and the damping from the noncritical load in series with ES, such oscillation is imperceptible in the grid's view, thus can be ignored for the power system simulation.

B. Phase II

As all the parameters of the order-reduced model have been estimated, the Phase II will validate the model. Fig. 10 shows the reconfigured system setup. The outer controller based on RCD control is employed to the smart load. Saturation has been set in all the PI controllers involved

1) $SatVol$ is set to limit the $V_{\rm esr}$, and thus to ensure the voltage of the noncritical load within the acceptable range.
2) $SatRad$ is set to avoid rotating the θ_o beyond the range (if no limits here, for example, an inductive reference may lead to capacitive by accident and results in unstable response).

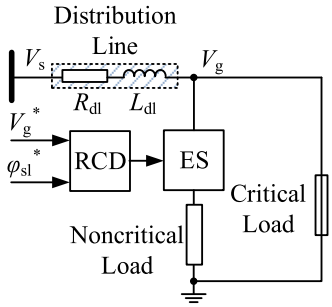

Fig. 10. System setup in phase II.

TABLE II
PHASE II SYSTEM SETUP PARAMETERS

V_s	V_g*	ω_s	R_{dl}	L_{dl}	L	C
110 V	110 V	100π rad/s	0.5 Ω	5 mH	0.6 mH	4.7 μF
K_{p1}	K_{i1}	K_{p2}	K_{i2}	$SatIn$	$SatVol$	$SatRad$
0.1	20	0.5	5	±30 V	±21 V	$\pm\pi$
P_0	Z_p	I_p	P_p	K_p	K_i	
373 W	0.81	0	0.19	0.1	25	

3) $SatIn$ is set to limit the final output of the ES, which ensures the inverter working in the rated operating region.

A distribution line emulator, comprising a resistor (R_{dl}) and an inductor (L_{dl}), has been inserted between the ac source and the smart load. Such configuration makes it possible to regulate the PCC voltage by adjusting the active/reactive power of the smart load.

The ZIP load model is also validated based on experimental measurements in this phase. By connecting an electric load in constant power mode with an ac/dc converter (with PFC), the load with constant power characteristic could be emulated in the experiment. Note that the energy efficiency of the converter is about $84(\pm 2)\%$ in experiment setup, the power loss consumption in practice is assumed to be constant and compensated. All the parameters are provided in Table II.

During the initialization of system, the ES is controlled to zero voltage output, which is equal to be bypassed in the load branch. At $t = 5$ s, the RCD control is enabled with preset $\varphi_{\rm sl}^* = 0\,({\rm rad})$, then it begins to compensate V_g by adjusting the $V_{\rm esr}$. At $t = 15$ s, $t = 25$ s, and $t = 35$ s, $\varphi_{\rm sl}^*$ step changes to 0.28, 0, and -0.28, respectively. Finally, at $t = 45$ s, the RCD control is disabled and ES is controlled back to zero output.

Fig. 11 shows the experimental results (labeled with subscript Exp) and the matched prediction results from both the theoretical (labeled with subscript Sim1) and estimated (labeled with subscript Sim2) models. As a result, during $t = 5-15$ s, the PCC voltage is regulated toward the reference voltage a little because the active power of the smart load is compressed, and no reactive power is involved in the operation. In the duration of $t = 15-25$ s and $t = 35-45$ s, the reactive power is introduced because the power angle reference changes. Hence, the smart load involves inductive and capacitive characteristics besides original resistive characteristic, and the PCC voltage drops and rises correspondingly. During the whole process, both prediction results of the theoretical and estimated models match with the experimental measurements very well, especially the rising and falling dynamics. The two models' results are still overlapped and have an MSE of 0.2456 on the ES voltage response. Consequently, the other results, namely V_g, $I_{\rm sl}$, $P_{\rm sl}$, and $Q_{\rm sl}$, successfully reflect experimental results. In conclusion, the theoretical and estimated order-reduced models combined with the ZIP load are validated by experiment in the condition of single device operation.

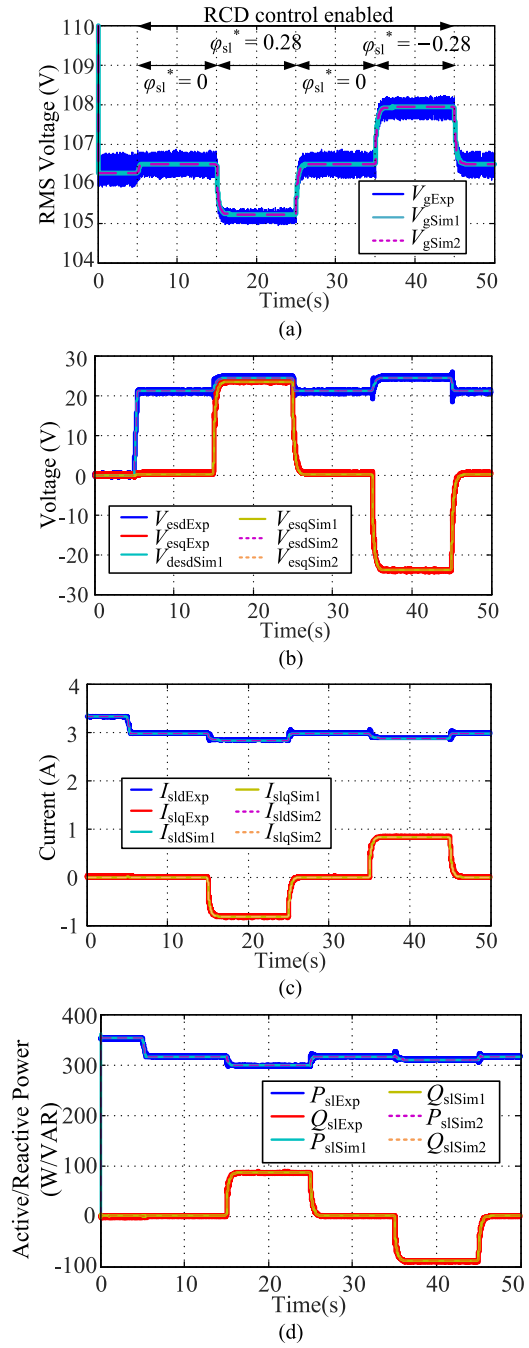

Fig. 11. Experimental and simulation results on Phase II setup with a ZIP load. (a) PCC Voltage (V_g). (b) Voltage output of ES $(V_{\rm es})$. (c) Current of the smart load $(I_{\rm sl})$. (d) *P*–*Q* power of the smart load.

TABLE III
THERMOSTATICALLY CONTROLLED LOAD PARAMETERS

τ_A	P_{PI}	I_{PI}	K_1	T_1	$G_{\max}$
25 °C	0.06	0.4	0.1	5 s	0.033 S

TABLE IV
PHASE III SYSTEM SETUP PARAMETERS

R_{dl1}	L_{dl1}	R_{dl2}	L_{dl2}	R_{dl3}	L_{dl3}
0.4 Ω	10.4 mH	0.4 Ω	5 mH	0.5 Ω	5 mH
ES1 K_{p1}	ES1 K_{i1}	ES1 K_{p2}	ES1 K_{i2}	ES2 K_{p1}	ES2 K_{i1}
0.1	20	0.5	5	0.1	20
ES2 K_{p2}	ES2 K_{i2}	ES3 K_{p1}	ES3 K_{i1}	ES3 K_{p2}	ES3 K_{i2}
0.5	5	0.1	10	0.1	1

Additionally, the dynamic thermostatic model is validated based on simulation results. The parameters of the thermostatically controlled load are listed in Table III. A small thermal time constant is selected for fast response and the other parameters about the system remains same.

Besides the same control references with the ZIP load test, the simulation requires an additional reference of the heated area temperature (τ^*), which is initialized to 40 °C and then step changes to 45 °C at $t = 20$ s. Fig. 12 shows the simulation results on both of the theoretical (labeled with subscript Sim1) and estimated (labeled with subscript Sim2) models. It is observed that before enabling the ES, during $t = 0-5$ s, the power of the load drops from the upper limit to a certain value due to the initial temperature difference. During $t = 5-25$ s, with ES enabled, the PCC voltage further drops because the thermostatic load reveals pure constant power characteristic in the stable state, which leaves compressing the $V_{\rm nc}$ by ES backfires. Introducing inductive load to the smart load or increasing τ^* in this period makes PCC voltage drop even severer. In the period of $t = 35-45$ s, the smart load is controlled to be resistive and capacitive again, and finally, to make the PCC voltage rise. Considering the simulation results from the models in the whole process and their strict overlap, it is clear that the proposed models could be also combined with dynamic loads and hence help to design the control method in such cases.

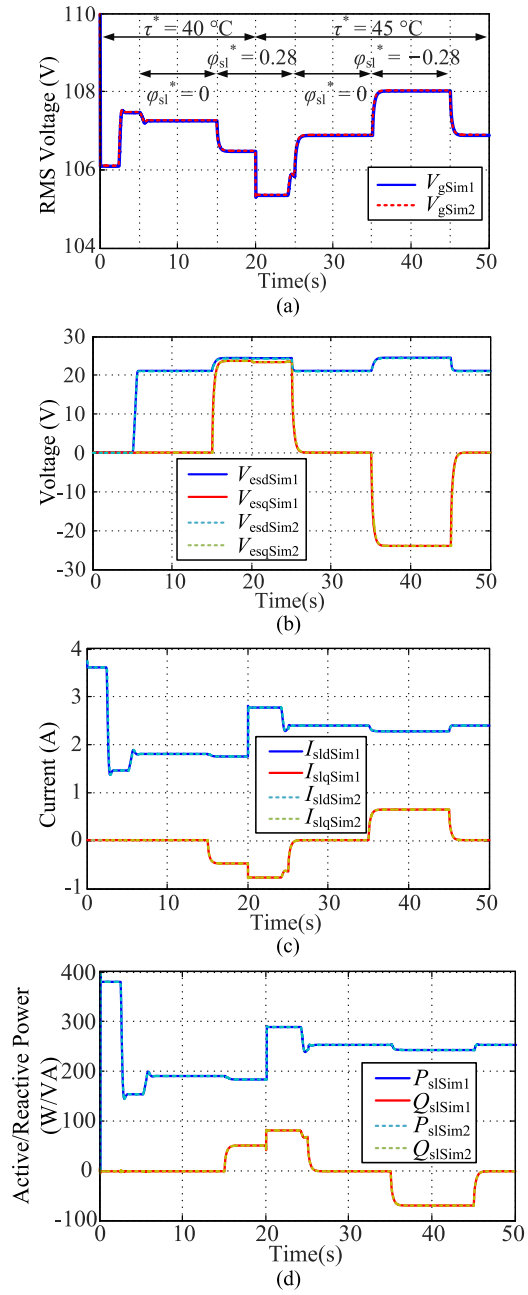

Fig. 12. Simulation results on Phase II setup with a thermostatic load. (a) PCC Voltage (V_g). (b) Voltage output of ES. $(V_{\rm es})$. (c) Current of the smart load $(I_{\rm sl})$. (d) *P*–*Q* power of the smart load.

C. Phase III

To further validate the models in the condition of multiple devices cooperation, three smart loads with ES embedded are connected to a micro power grid. Both the system diagram and the hardware setup are shown in Fig. 13. Updated parameters are provided in Table IV. The PI controller parameters controlling RCD power angle of ES3 are set differently from ES1 and ES2 for comparison. A dead zone of ±0.5 V is added to the PCC voltage control loops to avoid spurious triggering due to sensor noise. Since the responses of the theoretical and estimated models are strictly overlapped in the former phases, only the results of the estimated model are included in this phase.

After zero output initialization, at $t = 2$ s, the RCD control is enabled. The arbitrary presets of $\varphi_{\rm sl}^*$ for the three smart loads are -0.05, 0, and -0.05, respectively. Three smart loads try to regulate respective PCC voltages and quickly reach each static state. At $t = 10$ s, $\varphi_{\rm sl}{}^*$ for each of the smart loads step changes by -0.1. At $t = 18$ s, the RCD control is disabled, and the system returns to the initial state. Fig. 14 shows the experimental results (labeled with subscript Exp) and the matched simulation results of the estimated model (labeled with subscript Sim).

Obviously, after the RCD control is enabled, the PCC voltages of each smart load rise quickly. The PCC voltage of smart load 1 is regulated closely to the reference value, then enters the dead zone. At the same time, $V_{\rm esd}$ of ES2 and ES3 reaches the saturation but fails to regulate the respective PCC voltage

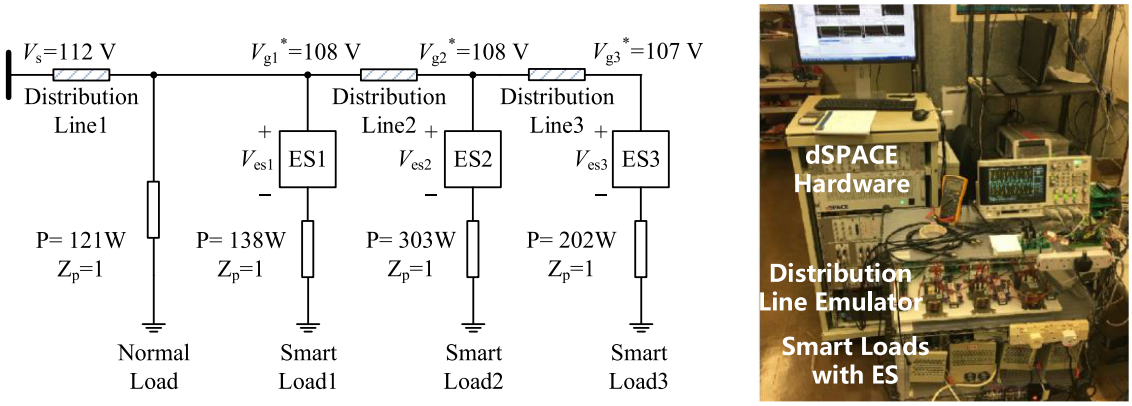

Fig. 13. System setup in phase III.

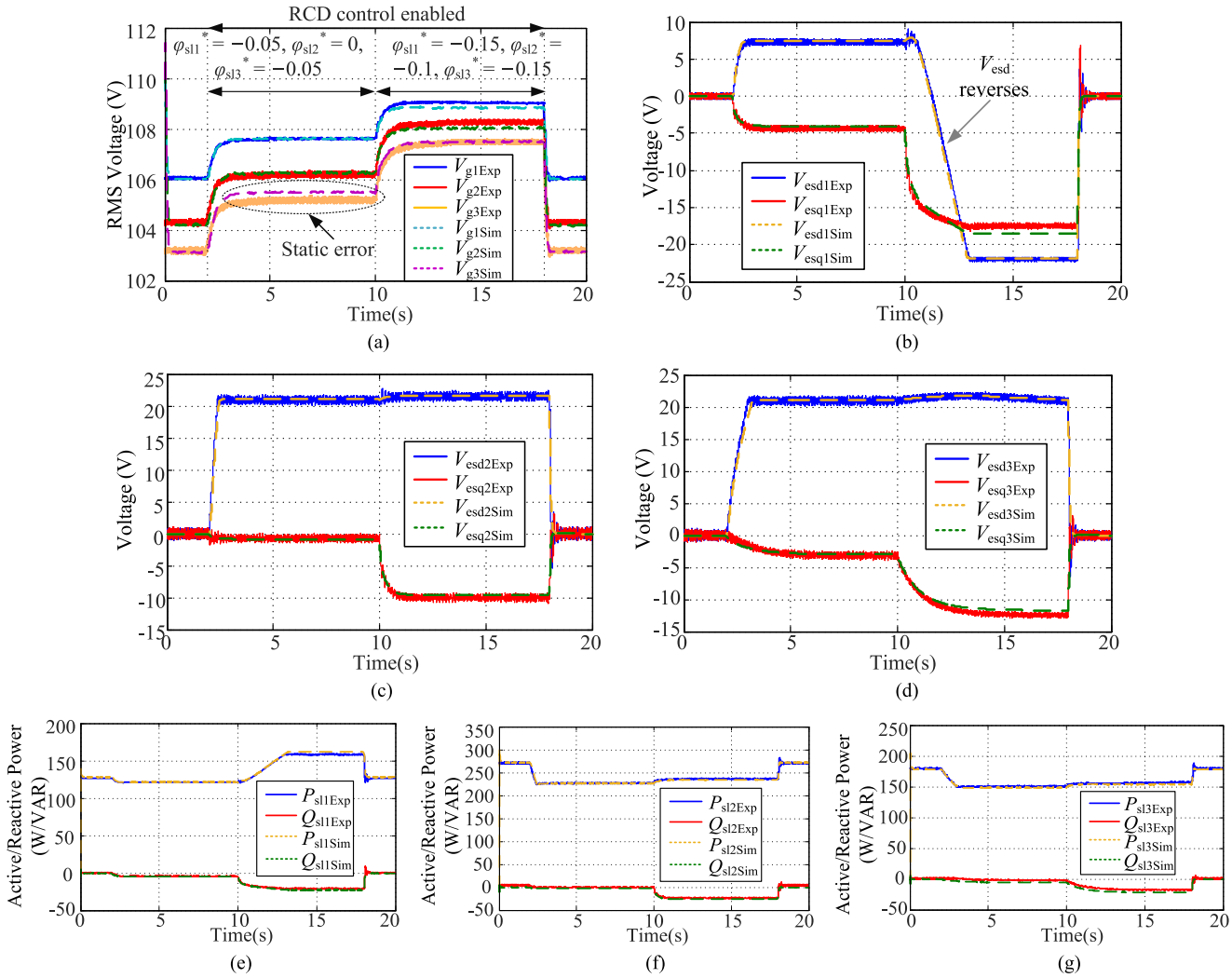

Fig. 14. Experimental and simulation results on phase III setup. (a) PCC voltage $(V_{g1/2/3})$. (b)Voltage output of ES 1 (V_{es1}). (c) Voltage output of ES 2 (V_{es2}). (d) Voltage output of ES 3 (V_{es3}). (e) *P*–*Q* power of smart load 1. (f) *P*–*Q* power of smart load 2. (g) *P*–*Q* power of smart load 3.

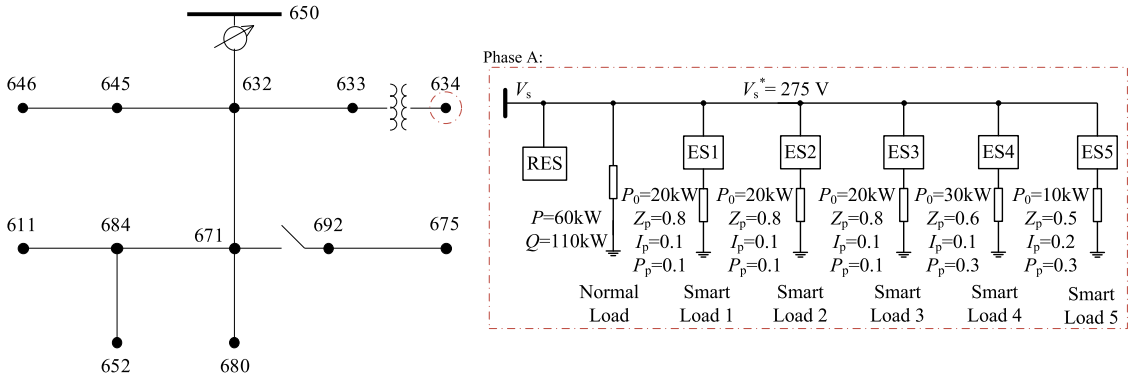

Fig. 15. Structure of the modified IEEE 13 node test feeder.

close enough to the reference values. During $t = 10-18$ s, with updated $\varphi_{\rm sl}^*$ reference, the PCC voltages of smart load 2 and 3 are finally regulated to the reference values. However, this results in the PCC voltage of the smart load 1 exceeding the upper limit of its controller's dead zone. Therefore, $V_{\rm esd}$ of the ES1 output works reversely to hold the V_{g1}. The PCC voltage of smart load 1 is finally stabilized within the preset range. Similar to the results of Phase II, the simulation results match very well with the experimental measurements. There is some static error. For instance, the max static error between measurement and simulation results of V_{g3} is -0.42 V, when the measured value of V_{g3} is about 105 V. Considering the measuring error for each component cannot be eliminated in practice, static error in this level is acceptable in such a system. As a result, the proposed model successfully predicts the practical measurement in this case. Hence, the proposed model is further validated on multiple device setup.

D. Phase IV

Phase IV demonstrates how the smart loads with ES interact with the grid based on certain strategy. The estimated order-reduced model is applied to an IEEE 13 node test feeder model. The modified system setup is shown as Fig. 15. As the smart load with ES is originally designed to be utilized in the residential customers, they are settled at Phase A of the load branch at node 634. A renewable energy source, which represents a residential solar system, is also involved in this branch.

As the renewable power injected is continuously varying, the power consumption monitored at Node 634 will be changing accordingly, which will not only affect the customer side voltage, but also influence the other node voltage if the power fluctuates severely. In this case, a group of smart loads with ES embedded try to compensate the active power fluctuation and regulate the PCC voltage. With the knowledge of the rated renewable energy and measuring energy injected to the grid, a simple control scheme to coordinate the smart loads with weight factor is shown as Fig. 16.

By adjusting the power angle, each smart load is able to adjust the power consumption in real time to keep the power consumption of the whole branch constant. The weight factor can be simply set based on the power value of the constant

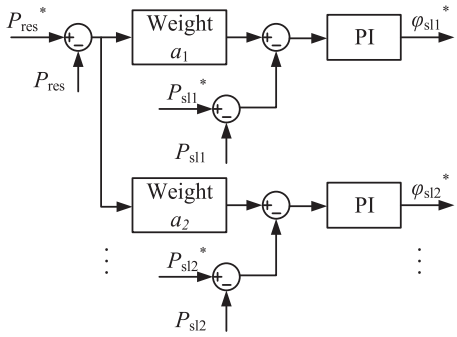

Fig. 16. Control scheme of the smart loads group.

impedance part of the ZIP loads, namely

$$a_i = \frac{P_{0,i} Z_{p,i}}{\sum_{n=1}^{m} P_{0,n} Z_{p,n}}. \tag{33}$$

Except the modified Node 634, all the other component parameters are the same as the IEEE document provided. The solar power injecting to the grid is amplified in scale and accelerated (to fit the simulation power level and show dynamic performance efficiently) based on practical measured solar irradiation data at Hamburg, Germany (latitude $= 53.513^\circ$, longitude $= 10.002^\circ$) on August 1, 2005 [30]. The controller parameters of each smart load are the same with the Phase II. Fig. 17 shows the simulation results. As the smart load 1, 2, and 3 share the same setup, their measured power are summed up and shown as a whole. It is observed that the PCC voltage and the total power of the branches are both well regulated comparing with the cases when ES is off.

This phase is a demonstration on applying the proposed model in a complex power system. The control strategy of the smart load could be flexible. The weight sharing control strategy is an example to show the effectiveness of voltage stabilization with the effort from smart loads with ES embedded.

E. Phase V

In this phase, a single smart load with ES associated is used to compensate both the voltage and frequency fluctuation in a balanced three-phase microgrid system by simulation. The

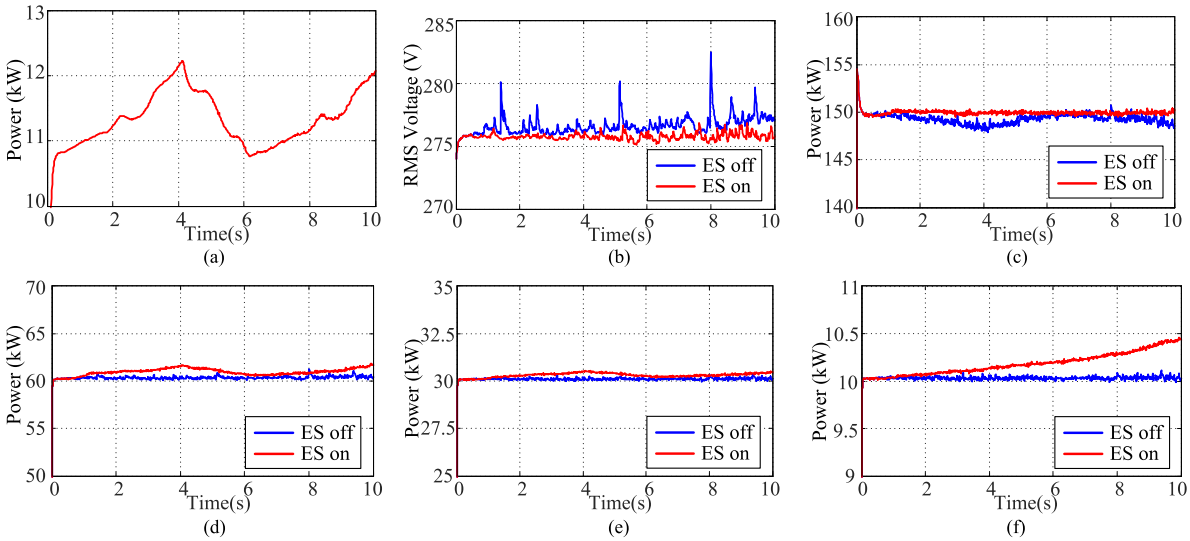

Fig. 17. Simulation results on phase IV setup. (a) Power delivered by the renewable energy source. (b) Phase A voltage of node 634 (V_s). (c) Power absorbed in phase A of node 634. (d) Sum power absorbed by smart load 1, 2, and 3. (e) Power absorbed by smart load 4. (f) Power absorbed by smart load 5.

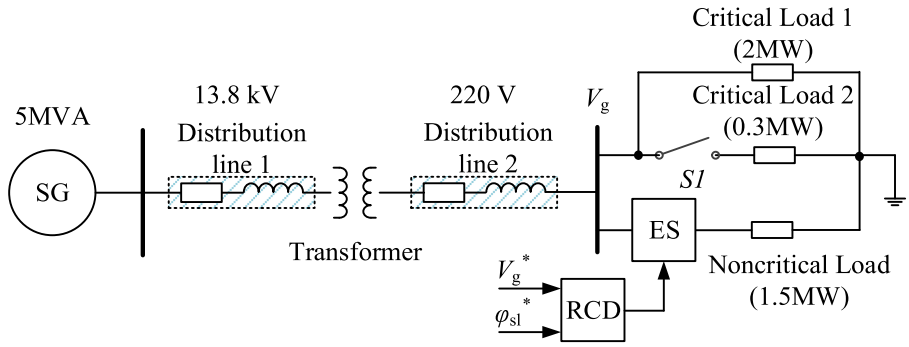

Fig. 18. System setup in phase V.

TABLE V
PHASE V SYSTEM SETUP SPECIFICATIONS

Distribution Line			
R_{dl1}	L_{dl1}	R_{dl2}	L_{dl2}
3.06 Ω	5.10 mH	0.3 mΩ	1.37 μH
Synchronous Machine			
Nominal Power	Line-to-line Voltage	Frequency	$[X_d, X_d', X_d'', X_q, X_q', X_q'']$ (p.u.)
5×10^6 VA	13.8×10^3 V	50 Hz	1.65,0.25,0.2,1.59,0.46,0.2,0.14
Stator Resistance	Inertia Coefficient	Pole pairs	$[T_{do}', T_{do}'', T_{qo}', T_{qo}'']$
0.0045Ω	3.2 s	1	4.5,0.04,0.67,0.09
Transformer			
Nominal Power	V1 Ph–Ph Votlage (rms)	V2 Ph–Ph Votlage (rms)	Windings Connection
5×10^6 VA	13.0×10^3 V	381 V	Delta to Star ground

system setup is shown in Fig. 18. A synchronous generator (with excitation system and a governor for basic droop control) delivers power to the demand-side via two parts of distribution line and a stepdown transformer. There are two critical loads and a smart load with ES associated on the demand-side. The key specifications are provided in Table V [12]. In the simulation with a period of 25 s, the Critical Load 2 connects to the grid when the switch $S1$ is closed at $t = 4$ s, which causes a sudden change of load power and corresponding fluctuations of voltage and frequency. Built with the proposed model, the ES is controlled to compensate both the fluctuation on voltage and frequency at the same time. The voltage reference V_g^* is

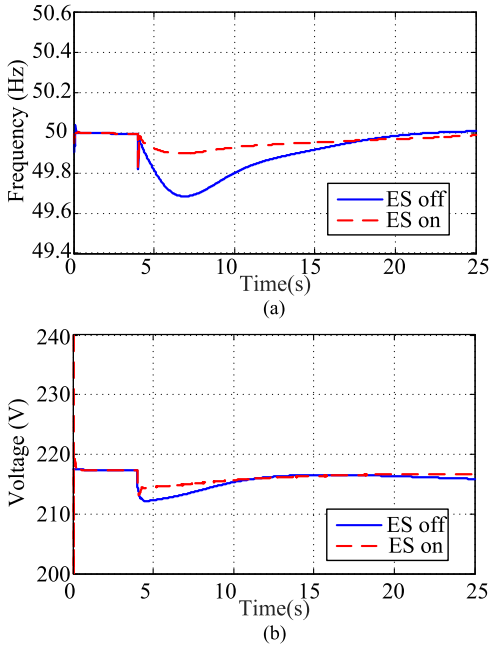

Fig. 19. Simulation results on phase V setup. (a) Utility frequency. (b) PCC voltage (V_g).

set to 215 V constantly. The power angle reference is set to 0 initially, then changed to 0.1 when the switch is closed, and reduced with a slope –0.006 per second until it reaches 0.

Fig. 19 shows the comparison results of the utility frequency and the PCC voltage from $t = 0-25$ s with ES on and off. As indicated by Fig. 19(a), compared with the frequency fluctuation with ES off, the deviation of frequency is significantly reduced and restored to an acceptable value faster with ES on. Similarly, reduced deviation and faster restoration of voltage are observed in Fig. 19(b). This demonstration shows that the proposed model can also be used in the condition with frequency fluctuation.

VI. Conclusion

In this paper, the dynamic model of an ES is first analyzed as a theoretical model in state space. An order-reduced model is derived by estimation based on experimental measurements. A theoretical model of the order of 6 with four inputs has been simplified into a second-order model with two inputs. The RCD control is adopted as the outer-controller module in the smart load. Two models of noncritical loads, namely ZIP and thermostatic load models, are analyzed to cooperate with the ES. The estimated ES model (the inner model), outer controller, and the load model can be modeled separately as modules and then combined to form the smart load model. The modular approach offers the flexibility of the proposed model in outer-controller design and the noncritical load selection. The results obtained from the proposed model are compared with experimental measurements in different setups for model verification. The proposed model has been tested for voltage and frequency regulation. This simplified modular modeling method could pave the way for future work on modeling widely distributed ESs in distribution networks so that various control strategies can be studied.

References

[1] J. M. Guerrero, J. C. Vasquez, J. Matas, M. Castilla, and L. G. de Vicuna, "Control strategy for flexible microgrid based on parallel line-interactive UPS systems," *IEEE Trans. Ind. Electron.*, vol. 56, no. 3, pp. 726–735, Mar. 2009.

[2] P. Khayyer and U. Ozguner, "Decentralized control of large-scale storage-based renewable energy systems," *IEEE Trans. Smart Grid*, vol. 5, no. 3, pp. 1300–1307, May 2014.

[3] Y. Yang, H. Wang, F. Blaabjerg, and T. Kerekes, "A hybrid power control concept for PV inverters with reduced thermal loading," *IEEE Trans. Power Electron.*, vol. 29, no. 12, pp. 6271–6275, Dec. 2014.

[4] A. H. Mohsenian-Rad, V. W. S. Wong, J. Jatskevich, R. Schober, and A. Leon-Garcia, "Autonomous demand-side management based on game-theoretic energy consumption scheduling for the future smart grid," *IEEE Trans. Smart Grid*, vol. 1, no. 3, pp. 320–331, Dec. 2010.

[5] A. J. Conejo, J. M. Morales, and L. Baringo, "Real-time demand response model," *IEEE Trans. Smart Grid*, vol. 1, no. 3, pp. 236–242, Dec. 2010.

[6] S. Y. Hui, C. K. Lee, and F. F. Wu, "Electric springs—A new smart grid technology," *IEEE Trans. Smart Grid*, vol. 3, no. 3, pp. 1552–1561, Sep. 2012.

[7] C. K. Lee, B. Chaudhuri, and S. Y. Hui, "Hardware and control implementation of electric springs for stabilizing future smart grid with intermittent renewable energy sources," *IEEE J. Emerg. Sel. Topics Power Electron.*, vol. 1, no. 1, pp. 18–27, Mar. 2013.

[8] S. C. Tan, C. K. Lee, and S. Y. Hui, "General steady-state analysis and control principle of electric springs with active and reactive power compensations," *IEEE Trans. Power Electron.*, vol. 28, no. 8, pp. 3958–3969, Aug. 2013.

[9] S. Yan *et al.*, "Extending the operating range of electric spring using back-to-back converter: Hardware implementation and control," *IEEE Trans. Power Electron.*, vol. 32, no. 7, pp. 5171–5179, Jul. 2017.

[10] Q. Wang, M. Cheng, and Z. Chen, "Steady-state analysis of electric springs with a novel δ control," *IEEE Trans. Power Electron.*, vol. 30, no. 12, pp. 7159–7169, Dec. 2015.

[11] K. T. Mok, S. C. Tan, and S. Y. Hui, "Decoupled power angle and voltage control of electric springs," *IEEE Trans. Power Electron.*, vol. 31, no. 2, pp. 1216–1229, Feb. 2016.

[12] T. Yang, K. T. Mok, S. C. Tan, and S. Y. R. Hui, "Electric springs with coordinated battery management for reducing voltage and frequency fluctuations in microgrids," *IEEE Trans. Smart Grid*, vol. 9, no. 3, pp. 1943–1952, May 2018.

[13] Q. Wang, M. Cheng, and Y. Jiang, "Harmonics suppression for critical loads using electric springs with current-source inverters," *IEEE J. Emerg. Sel. Topics Power Electron.*, vol. 4, no. 4, pp. 1362–1369, Dec. 2016.

[14] S. Yan, S. C. Tan, C. K. Lee, B. Chaudhuri, and S. Y. R. Hui, "Electric springs for reducing power imbalance in three-phase power systems," *IEEE Trans. Power Electron.*, vol. 30, no. 7, pp. 3601–3609, Jul. 2015.

[15] Y. Zheng, D. J. Hill, K. Meng, and S. Y. R. Hui, "Critical bus voltage support in distribution systems with electric springs and responsibility sharing," *IEEE Trans. Power Syst.*, vol. 32, no. 5, pp. 3584–3593, Sep. 2017.

[16] N. R. Chaudhuri, C. K. Lee, B. Chaudhuri, and S. Y. R. Hui, "Dynamic modeling of electric springs," *IEEE Trans. Smart Grid*, vol. 5, no. 5, pp. 2450–2458, Sep. 2014.

[17] Y. Yang, S. S. Ho, S. C. Tan, and S. Y. R. Hui, "Small-signal model and stability of electric springs in power grids," *IEEE Trans. Smart Grid*, vol. 9, no. 2, pp. 857–865, Mar. 2018.

[18] S. Zhang and D. Qiu, "Study on the characteristics of electric spring with nonlinear load," in *Proc. 2016 IEEE 8th Int. Power Electron. Motion Control Conf.*, 2016, pp. 3284–3289.

[19] A. J. Collin, G. Tsagarakis, A. E. Kiprakis, and S. McLaughlin, "Development of low-voltage load models for the residential load sector," *IEEE Trans. Power Syst.*, vol. 29, no. 5, pp. 2180–2188, Sep. 2014.

[20] A. Bokhari *et al.*, "Experimental determination of the ZIP coefficients for modern residential, commercial, and industrial loads," *IEEE Trans. Power Del.*, vol. 29, no. 3, pp. 1372–1381, Jun. 2014.

[21] P. Kundur, N. J. Balu, and M. G. Lauby, *Power System Stability and Control*, vol. 7. New York, NY, USA: McGraw-Hill, 1994, pp. 274–268.

[22] Distribution System Analysis Subcommittee, "IEEE 13 node test feeder," 2000. [Online]. Available: https://ewh.ieee.org/soc/pes/dsacom/testfeeders/

[23] C. K. Lee, H. Liu, G. Zhang, S. Yan, E. Waffenschmidt, and S. Y. R. Hui, "A unified converter topology for electric spring," in *Proc. 2016 IEEE 7th Int. Symp. Power Electron. Distrib. Gener. Syst.*, 2016, pp. 1–6.

[24] C. Cai, Z. Wang, J. Xu, and Y. Zou, *Finite Frequency Analysis and Synthesis for Singularly Perturbed Systems*. New York, NY, USA: Springer, 2016, pp. 16–21.
[25] M. G. Safonov, E. A. Jonckheere, M. Vermaj, and D. J. N. Limebeer, "Synthesis of positive real multivariable feedback systems," *Int. J. Control*, vol. 45, no. 3, pp. 817–842, Mar. 1987.
[26] M. Dahleh, M. A. Dahleh, and G. Verghese, *Lectures on Dynamic Systems and Control*. Cambridge, MA, USA: MIT Press, course 6.241, ch. 12.
[27] J. R. Schott, *Matrix Analysis for Statistics*. New York, NY, USA: Wiley, 2016, pp. 175–178.
[28] L. Ljung, *System Identification: Theory for the User*, 2nd ed. Upper Saddle River, NJ, USA: Prentice-Hall, 1999, pp. 197–203, 326–329.
[29] "Estimate state-space model using time or frequency domain data - MATLAB ssest," 2000. [Online]. Available: https://www.mathworks.com/help/ident/ref/ssest.html
[30] "Solar radiation data Service," 2014 [Online]. Available: http://www.soda-pro.com/web-services/radiation/helioclim-3-for-free/

Tianbo Yang (S'15) received the B.Eng. and M.Phil. degrees in automation and control engineering from the Harbin Institute of Technology, Harbin, China, in 2012 and 2014, respectively. He is currently working toward the Ph.D. degree in electrical engineering at the Department of Electrical and Electronic Engineering, the University of Hong Kong, Hong Kong.

His research interests include power electronic technologies in smart grid and energy storage system.

Tao Liu (M'13) received the B.E. degree in automation from Northeastern University, Shenyang, China, in 2003, and the Ph.D. degree in engineering from the Australian National University, Canberra, ACT, Australia, in 2011.

In 2012, he was a Research Fellow with the Research School of Engineering, the Australian National University, for five months. He also held a Visiting Scholar position with the Centre for Future Energy Networks, University of Sydney, Sydney, NSW, Australia. From 2012 to 2013, he was a Postdoctoral Fellow with the University of Groningen, Groningen, The Netherlands. In 2013, he moved to the University of Hong Kong, Hong Kong, where he was a Postdoctoral Fellow until 2015. He is currently a Research Assistant Professor with the Department of Electrical and Electronic Engineering, University of Hong Kong. His research interests include power systems, dynamical networks, distributed control, event-triggered control, and switched systems.

Jie Chen (S'17) received the B.Eng. degree in electronic information and electrical engineering from the Shanghai Jiao Tong University, Shanghai, China, in 2015. He is currently working toward the Ph.D. degree in electrical engineering at Power Electronics Research Group, Department of Electrical and Electronic Engineering, The University of Hong Kong, Hong Kong.

His research interests include smart grid technologies, electric springs, and consensus control.

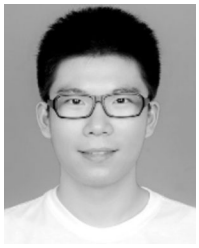

Shuo Yan (S'13–M'16) received the B.Eng. degree from The University of South China, Hengyang, China, in 2007, the M.Eng. degree at Southeast University, Nanjing, China, in 2010, and the Ph.D. degree from The University of Hong Kong, Hong Kong, in 2016, all in electrical engineering.

He is currently a Postdoctoral Research Fellow with the Department of Electrical and Electronic Engineering, The University of Hong Kong. His current research interests include power electronic technologies, smart grid, renewable energy, and microgrids.

S. Y. Ron Hui (M'87–SM'94–F'03) received the B.Sc. (Eng. Hons.) in electrical and electronic engineering from the University of Birmingham, Birmingham, U.K., in 1984, and the D.I.C. and Ph.D. degree in electrical engineering from Imperial College London, London, U.K., in 1987.

He is a Chair Professor of Power Electronics with the University of Hong Kong, Hong Kong, and concurrently holds a part-time Chair Professorship with Imperial College London. He has authored and coauthored more than 400 technical papers, including more than 250 refereed journal publications and book chapters. More than 60 of his patents have been adopted by industry. His inventions on wireless charging platform technology underpin key dimensions of Qi, the world's first wireless power standard, with freedom of positioning and localized charging features for wireless charging of consumer electronics.

Dr. Hui is the recipient of the 2010 IEEE Rudolf Chope R&D Award from the IEEE Industrial Electronics Society, the 2010 IET Achievement Medal (The Crompton Medal), and the 2015 IEEE Technical Field Award (IEEE William E. Newell Power Electronics Award). He is a Fellow of the Australian Academy of Technological Sciences and Engineering, and also the Royal Academy of Engineering, U.K.